

SOFT ROBOTS

High-load capacity origami transformable wheel

Dae-Young Lee^{1,2}, Jae-Kyeong Kim¹, Chang-Young Sohn³, Jeong-Mu Heo³, Kyu-Jin Cho^{1*}

Composite membrane origami has been an efficient and effective method for constructing transformable mechanisms while considerably simplifying their design, fabrication, and assembly; however, its limited load-bearing capability has restricted its application potential. With respect to wheel design, membrane origami offers unique benefits compared with its conventional counterparts, such as simple fabrication, high weight-to-payload ratio, and large shape variation, enabling softness and flexibility in a kinematic mechanism that neutralizes joint distortion and absorbs shocks from the ground. Here, we report a transformable wheel based on membrane origami capable of bearing more than a 10-kilonewton load. To achieve a high payload, we adopt a thick membrane as an essential element and introduce a wireframe design rule for thick membrane accommodation. An increase in the thickness can cause a geometric conflict for the facet and the membrane, but the excessive strain energy accumulation is unique to the thickness increase of the membrane. Thus, the design rules for accommodating membrane thickness aim to address both geometric and physical characteristics, and these rules are applied to basic origami patterns to obtain the desired wheel shapes and transformation. The capability of the resulting wheel applied to a passenger vehicle and validated through a field test. Our study shows that membrane origami can be used for high-payload applications.

INTRODUCTION

Origami has been a rich source of inspiration for art, education, and mathematics, and it has proven to be an efficient and effective method for realizing transformable structures in nature (1–3) and artificial systems (4–8). Composite membrane origami, the design technique based on the laminar composition of flexible membranes with rigid facet constraints, opens a new field for robotics by the transition from component assembly to lamination, which considerably simplifies design, fabrication, and assembly. This transition simplifies and speeds up fabrication and enables reaching size scales that were difficult to access before (9, 10). In addition, membrane origami provides a versatile shape-changing ability that has been exploited in various applications (11–15), and its applicability has been extended by additional design dimensions obtained from material characteristics such as softness and stretchability (16–19).

Beyond the aforementioned benefits, origami has been an effective design tool for constructing a high payload-to-weight structure, such as a honeycomb panel, by markedly increasing the buckling strength using unique geometric configurations (20, 21). Combining this feature with reconfigurability, various stiffness transition mechanisms have also been introduced (22–24). The rigidity of components is another important factor to secure high load capacity and closely related to the thickness. Origami design is, traditionally, a matter of organizing fold lines under fundamental and ideal assumptions—zero facet thickness and zero fold line width (25–27). However, in response to growing interest in origami-inspired applications that require load-bearing capability, various thickness accommodation methods have been introduced (28–30).

Here, we examine a special load-bearing problem that cannot be solved by the aforementioned load-bearing design techniques: a wheel that can be transformable and should withstand a high load

all through, even in the shape-transition state. In a previous study, we reported an origami design method for a transformable wheel (31). By introducing flexible facets, it was possible to achieve a degree of freedom that enables shifting between different wheel shapes; however, there was a limitation in its load-bearing capacity. The difficulty of high load bearing in a transition state comes from the variation in the stress distribution. In general, the joint membrane is vulnerable compared with the rigid facet, but it is possible to make the facet bear most of the stress through the structural design (23, 24). However, an arbitrary configuration in the transition state places high stress on all components so that the tensile load capacity of the membrane determines the load capacity of the overall system.

To solve this issue, we introduce a wireframe design rule for thick membrane accommodation. Unlike the facet, the membrane experiences a large deformation in shape transition so that the increase in membrane thickness can cause geometric conflict and excessive strain energy accumulation. Thus, the design rules for accommodating membrane thickness aim to address both geometric and physical characteristics, and these rules are applied to basic origami patterns to obtain the desired wheel shapes and transformation. As a result, we demonstrate a transformable wheel with extreme load-bearing capability that can be applied to a passenger vehicle. With the high load capacity, the developed composite membrane origami provides softness and flexibility to the wheels in the kinematic mechanism, thus neutralizing distortions and absorbing shocks from the ground. Other benefits of the origami method—including fabrication efficiency (420 joint structures assembled within 4 hours), payload-to-weight ratio (>50), and shape variation ratio (~1.7)—are also demonstrated with the target scale.

RESULTS

The wheel can transform into two shapes—a large protruding wheel and a small smooth wheel—by folding and unfolding the spokes through adjustments in the distance between the wheel hub plates (Fig. 1A). Therefore, the wheel width and diameter vary depending on the configuration, as illustrated in Fig. 1B, with the diameter

Copyright © 2021
The Authors, some
rights reserved;
exclusive licensee
American Association
for the Advancement
of Science. No claim
to original U.S.
Government Works

¹Biorobotics Lab, Soft Robotics Research Center, School of Mechanical Engineering/IAMD, Institute of Engineering Research, Seoul National University, Seoul, Republic of Korea. ²School of Engineering and Applied Sciences, Harvard University, Cambridge, MA, USA. ³R&D Center, Hankook Tire and Technology Co. Ltd., Daejeon, Republic of Korea.

*Corresponding author. Email: kjcho@snu.ac.kr



Fig. 1. Transformable wheel concept and demonstration. (A) The wheel can be transformed into two shapes according to the road condition. (B) The relationship between the diameter and width of the wheel. (C) The load-displacement response of the wheel in the shape-transition state. (D) We designed a single-passenger vehicle for installation of the transformable wheels. The operation and capacity of the wheels were demonstrated through a field test.

varying from 0.46 to 0.8 m. We verified the load-bearing capacity of one wheel through experiments with cyclic loads of 5 ± 2 , 7 ± 2 , and 9 ± 2 kN in the shape-transition state. The wheel performance is maintained for loads below 11 kN, as shown in Fig. 1C. The detailed conditions and results of these experiments are available in the Supplementary Materials. We installed the developed transformable wheels on a single-passenger vehicle that was specially designed for independently transmitting torque for wheel rotation and force for wheel transformation (Fig. 1D).

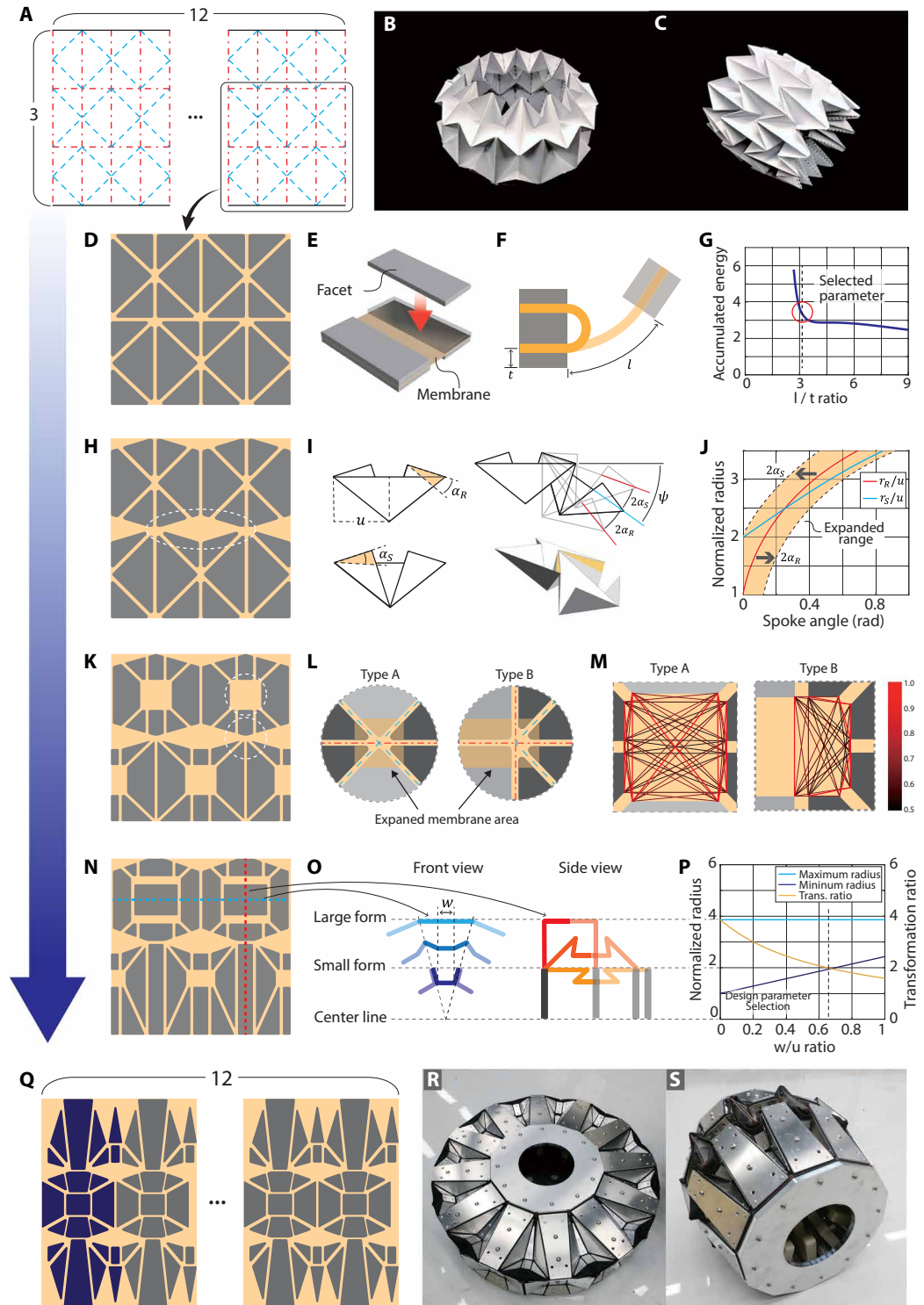
The shape-shifting wheel concept has been implemented by various origami patterns (32–34). We chose the waterbomb tessellation origami pattern, whose characteristics have been analyzed in (35–38), as a springboard for the wheel design due to the following reasons: The waterbomb-based wheel structure can have perpendicularity in directions of driving transformation (horizontal) and supporting payload (vertical). This configuration makes it possible to maintain the two different shapes with minimum energy input. The L beam-shaped spoke is another advantage of the waterbomb pattern that can increase the buckling resistance of the structure. To transfer the paper model into a heavy-duty wheel prototype, we applied the stepwise design approach, and the overall procedure is illustrated

in Fig. 2. The paper model of the wheel is made of 3×12 repetitions of a basic pattern (Fig. 2, A to C). The transition from the paper model into a composite membrane is achieved by anchoring rigid facets to a flexible membrane (Fig. 2, D and E), with the default length of the membrane gap, l , being the main design parameter at this stage. Given the simple folding with two facets, the minimum l would be twice the thickness of the facet for flat foldability. However, a thick membrane with high curvature induces considerable resistance force and energy accumulation. On the other hand, increasing l makes the entire structure deviate from the desired shape. To select an appropriate interval for this parameter, we use the Euler-Bernoulli beam theory to estimate the accumulated energy according to l (Fig. 2, F and G) (39). The details about the corresponding parameter selection are available in Supplementary Text.

Securing the kinematical degrees of freedom is the next stage of the pattern design. The waterbomb tessellation pattern creates a dependency between the wheel diameter and spoke angle ψ , which is depicted as the red curve in Fig. 2J. Moreover, the connection between the wheel hub and spoke facet creates an additional dependency, depicted as the blue curve. This conflict causes an overconstraint, but it can be solved by expanding the flexible area as reported in the

Fig. 2. Pattern transition from paper model to wheel prototype.

(A) Waterbomb tessellation pattern for the wheel. (B) Paper model of the wheel in large form. (C) Paper model of the wheel in small form. (D) Origami composite of the waterbomb pattern. (E) Composite composition. (F) Schematic of origami composite (lateral view). (G) Variation of the accumulated energy on membrane according to membrane length (l)–to–facet thickness (t). (H) Origami composite pattern variation to solve over-constraint issues. (I) Geometrical description of wheel unit structures. (J) Relationship between the wheel radius and spoke angle. The shaded area in the graph indicates the variable range of the radius according to the expanded membrane area. (K) Origami composite pattern variation for accommodation of thickness. (L) Two types of the vertexes and the shapes of the expanded membrane. (M) The wires that connect vertexes represent the membrane, and the wire color indicates the length ratio between the unfolded and folded states. (N) Origami composite pattern variation considering payload and transformation ratio. (O) Schematic of the front view and side view of the wheel. (P) Relationship between the wheel radius, the transformation ratio, and the central pattern width (w). (Q) Final pattern of the transformable wheel and (R and S) the implementation results of the wheel. The diameter of the wheel in large form is ~ 0.75 m, and that in small form is ~ 0.4 m.



previous study (31). The expanded flexible area (Fig. 2H) produces an additional degree of freedom with the angle range of α_R and α_S (Fig. 2I), corresponding to the light yellow region in Fig. 2J. This relationship can be derived from the kinematical analysis of the wheel structure. The wheel structure consists of a rim part that makes the outer edge of the wheel and a spoke part that connects a wheel hub and the rim part (Fig. 3A). From the geometrical conditions shown in Fig. 3 (B and C), the position vector of the vertices according to the wheel center frame, O - xyz , can be calculated as

$$\vec{p}_A = \left(0, 0, u \frac{\sin(\phi - \pi/12)}{\sin(\pi/12)} \right) \quad (1)$$

where

$$\vec{p}_B = \left(u, -\sin \phi, u \left\{ \frac{\sin(\phi - \pi/12)}{\sin(\pi/12)} + \cos \phi \right\} \right) \quad (2)$$

$$\vec{p}_C = \left(u \cos \phi, 0, u \left\{ \frac{\sin(\phi - \pi/12)}{\sin(\pi/12)} + \sin 2\xi \right\} \right) \quad (3)$$

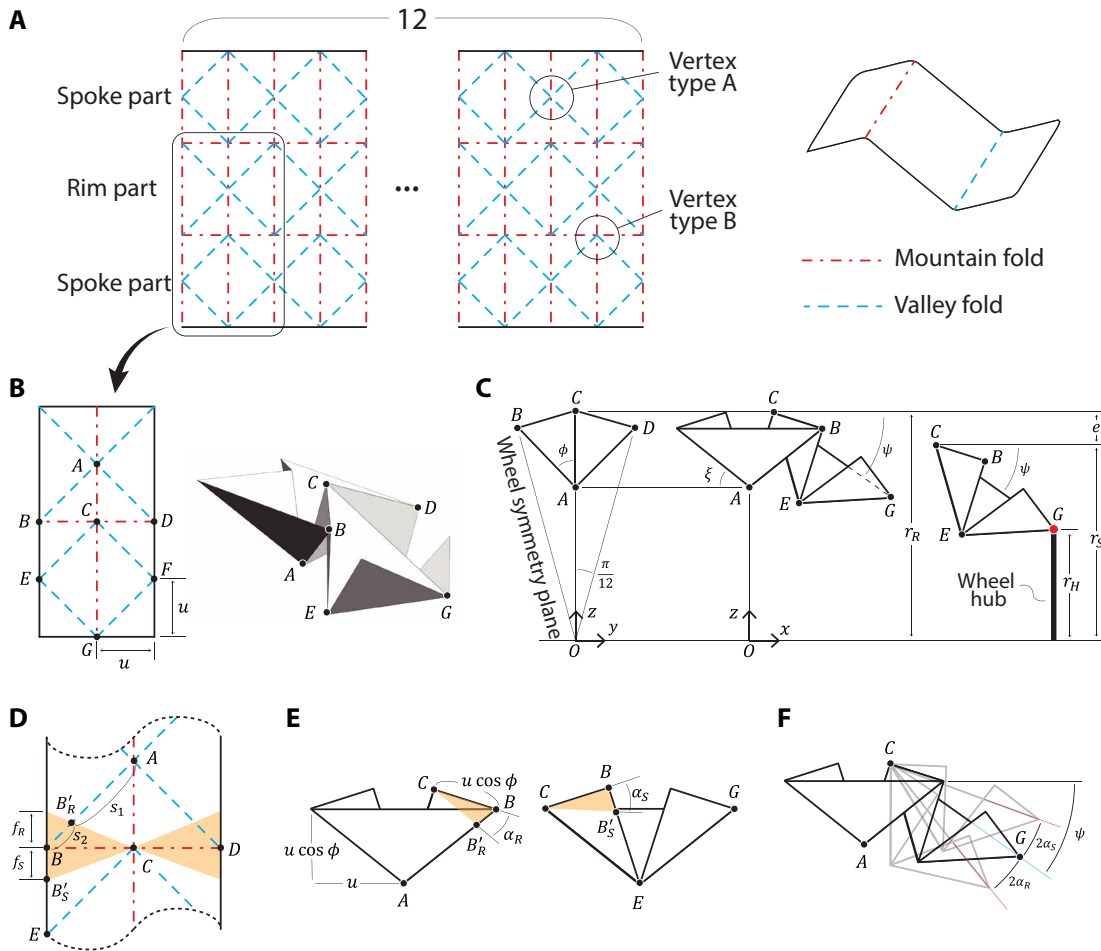


Fig. 3. Geometrical descriptions for kinematic analysis. (A) Folding pattern of the paper model of the wheel. The wheel consists of a central rim part and spoke parts on both sides. (B) Vertex configuration and its folded shape. (C) Geometrical description of the wheel model. The reference frame O - xyz represents the center of the wheel. (D) Modified vertex configuration with the expanded flexible area. The light yellow region represents a flexible area. (E) Geometrical description of the flexible area and its angle. (F) The range of the additional movement angle in the folded state.

$$\xi = \tan^{-1}(\cos \phi) \quad (4) \quad \text{whereas}$$

and the z position of \vec{p}_C can be defined as a radius of the wheel

$$r_R = u \left\{ \frac{\sin(\phi - \pi/12)}{\sin(\pi/12)} + \sin 2\xi \right\} \quad (5)$$

The vertex E should be on the symmetry plane, which reduces the dimension of the vector to two so that it can be described as

$$\vec{p}_E = \left(\eta_{E1}, -\eta_{E2} \sin \frac{\pi}{12}, \eta_{E2} \cos \frac{\pi}{12} \right) \quad (6)$$

These two variables can be specified using the following constraints on the distance between the vertices

$$\|\vec{p}_B - \vec{p}_E\| = u, \|\vec{p}_C - \vec{p}_E\| = u\sqrt{2} \quad (7)$$

Similar to \vec{p}_E , the position vector of G can be derived as

$$\vec{p}_G = (\eta_{G1}, 0, \eta_{G2}) \quad (8)$$

$$\|\vec{p}_C - \vec{p}_G\| = 2u, \|\vec{p}_E - \vec{p}_G\| = u\sqrt{2} \quad (9)$$

The spoke angle, ψ , can be calculated from the result

$$\psi = \tan^{-1} \frac{z_C - z_G}{x_G - x_C} \quad (10)$$

Separately, the vertex G should be connected with the wheel hub (Fig. 3C), and the radius of the wheel can be calculated as

$$r_S = r_H + 2u \sin \psi \quad (11)$$

and the difference between r_R and r_S causes kinematic conflict represented by the errors, e

$$e = r_R - r_S \quad (12)$$

This error can be compensated by expanding the flexible area with the design parameters f_R and f_S in Fig. 3D. The position vector

of B'_R and B'_S can be calculated by the internal division of the line segment as follows

$$\overrightarrow{AB'_R} : \overrightarrow{B'_R B} = u : f_R \tag{13}$$

$$\overrightarrow{p_{B'_k}} = \frac{f_R \overrightarrow{p_A} + u \overrightarrow{p_B}}{u + f_R} \tag{14}$$

$$\overrightarrow{EB'_S} : \overrightarrow{B'_S B} = u - f_S : f_S \tag{15}$$

$$\overrightarrow{p_{B'_s}} = \frac{f_S \overrightarrow{p_A} + (u - f_S) \overrightarrow{p_B}}{u} \tag{16}$$

By projecting B'_R and B'_S to yz plane, angle boundaries of additional degrees of freedom, α_R and α_S , can be derived (Fig. 3, E and F). Figure 2J shows how an extended flexible area handles kinematic errors. The flexibility on the value of r_R achieved by α_R and α_S allows full containment of the profile of r_S . The simulation uses the following conditions

$$r_H/u = 2, f_R/u = 0.05, f_S/u = 0.05 \tag{17}$$

The design rule for accommodating the thickness of facet and membrane is applied to the pattern. The waterbomb tessellation is

composed of two types of vertices with six folds (Fig. 2L). Although both geometries satisfy the Kawasaki-Justin theorem for flat foldability, the theorem is based on a zero-thickness idealization, and the physical model with its thick components cannot achieve flat foldability. Similar to the single-fold problem, we expand the membrane area to accommodate its thickness considering both the geometrical conflict and strain energy accumulation on the membrane. Given the complex geometrical deformation of the membrane, obtaining an analytical model is difficult, whereas finite element analysis implies a high computational cost. Because design rules should allow preventing excessive energy accumulation, we establish a design rule by simplifying the membrane as a wireframe and predicting its overstretching without predicting the membrane behavior precisely. The wire-length ratio between the unfolded and folded states can be expressed graphically to obtain a design guideline representing the ratio by colors, as shown in Fig. 2M.

Figure 4 shows a graphical illustration of a wireframe-based design rule for accommodating thickness in consideration of both geometrical and physical characteristics. In a folded configuration of the type A vertex, $F1$ and $F4$ overlap $F2, F3, F5,$ and $F6$, which incur an offset in out-of-plane direction between $F1$ and $F4$ (Fig. 4A). This discrepancy can be accommodated by expanding a membrane area, and the expanded geometry and dimension of the area can be determined by the following steps. The first step is to

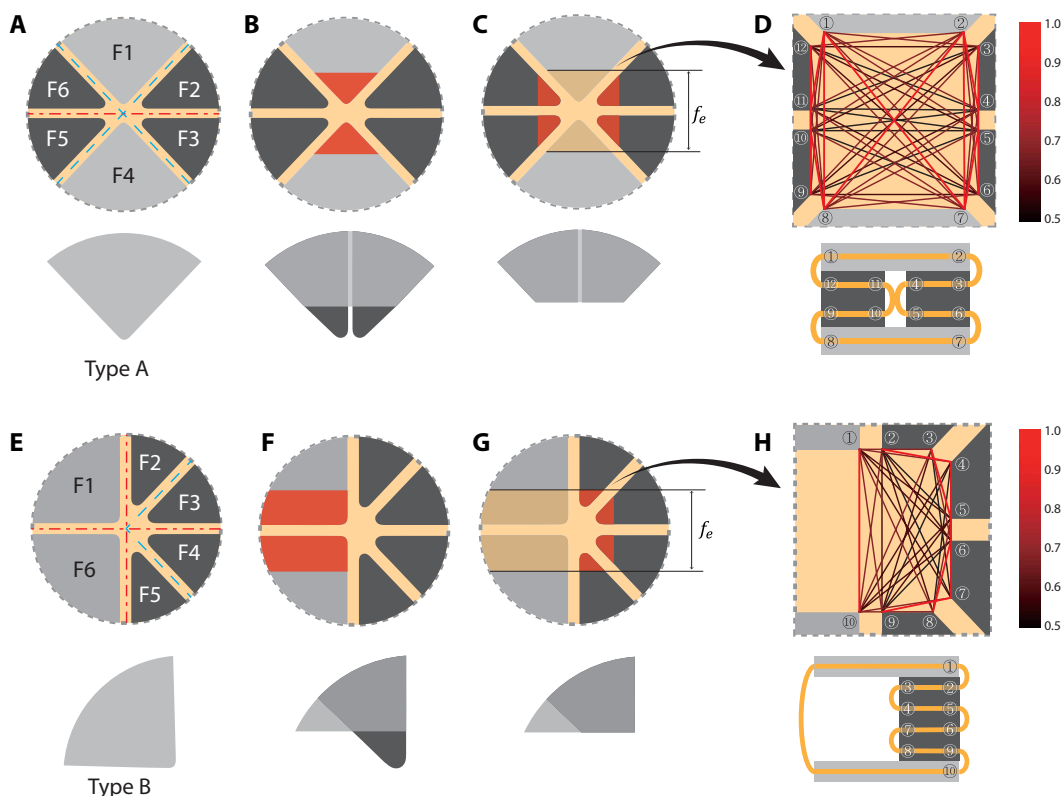


Fig. 4. Geometrical descriptions for thickness accommodation. (A) The geometry of type A vertex and its folded shape. The light gray color of the facet represents the outer side, and the dark gray represents the inner side. (B) Expansion of the membrane area to compensate for the distances between the outer facets, which are highlighted by the red color on the facet. (C) Additional membrane area expansion to solve the interference problem. (D) Graphical map of the wireframe for type A vertex. The color of the wire represents the length ratio between the unfolded and folded states. (E) The geometry of type B vertex and its folded shape. (F) Expansion of the membrane area to compensate for the distances between the outer facets, which are highlighted by the red color on the facet. (G) Additional membrane area expansion to solve the interference problem. (H) Graphical map of the wireframe for type B vertex.

draw lines on $F1$ and $F4$ that are parallel to the virtual fold line, the direction of the rotation vector between $F1$ and $F4$. By partially removing the facets based on these lines as described in Fig. 4B, the expanded membrane can reach both facets without stretching. However, in the folded state, $F2$, $F3$, $F5$, and $F6$ obstruct this connection, and these parts should be cleared as in Fig. 4C. As a result of expanding the membrane area, the single vertex in the original pattern was divided into 12 subvertices.

The design parameter for the expanded membrane region, f_e , was determined using a wireframe model. We can imagine virtual wires that connect each vertex, and the length of these wires will change as the model folds. The length of the wire between i th subvertex and j th subvertex can be presented as n_{ij} in the unfolded state, which is a function of the design variables l and e . Similarly, the wire length in the folded state can be represented as c_{ij} , and this is a function of t_m , t_f , and f_e . The supplementary length, w_s , is introduced to prevent the high curvature of the membrane. From these variables, the design criteria value, γ , and the condition can be defined as follows

$$\gamma_{ij} = \frac{c_{ij}(t_m, t_f, f_e) + w_s}{n_{ij}(l, f_e)} < 1 \quad (18)$$

From this condition, f_e can be determined on the basis of t_m , t_f , l , and w_s , and the result is presented in a graphical map as in Fig. 4D with the following simulation parameters

$$\begin{aligned} t_m/u = 0.1, t_f/u = 0.1, l/(0.5t_m + t_f) = \\ \pi, w_s/(0.5t_m + t_f) = \pi - 2, f_e/u = 0.4 \end{aligned} \quad (19)$$

The identical design rule can be used for the vertex type B in Fig. 4E. $F1$ and $F6$ enclose $F2$ to $F5$ with a different configuration. Similar to the type A vertex, the two parallel lines can be drawn with the desirable distance for covering inner facets as shown in Fig. 4F, and interference of $F2$ to $F5$ can be solved by removing the part of these facets (Fig. 4G). The result is presented in a graphical map as in Fig. 4H with the following simulation parameters

$$\begin{aligned} t_m/u = 0.1, t_f/u = 0.1, l/(0.5t_m + t_f) = \\ \pi, w_s/(0.5t_m + t_f) = \pi - 2, f_e/u = 0.6 \end{aligned} \quad (20)$$

We applied an additional pattern variation to reinforce the structure and adjusted the wheel transformation ratio, which is determined by design parameter w , as shown in Fig. 2O. A larger w is preferable to obtain a higher payload, but it reduces the transformation ratio, as described in Fig. 2 (O and P). w should be determined on the basis of a target payload, but analyzing the failure mode of the wheel is a challenging problem owing to its complex composition; the

structure is built by assembling various materials and could fail for a variety of reasons, such as exceeding the tensile strength of materials, structural buckling, or disassembly of parts. In this study, a simplified static model was used to estimate the applied load to the components (fig. S2 and Supplementary Text). When the target payload is 10 kN, the required load capacity for components is 28.8 kN, and the dimension of components was determined on the basis of this criterion. Figure 2Q illustrates the final pattern of the wheel. The top and bottom edges of the wheel pattern are connected to the wheel hub. To reinforce the connection between the wheel pattern and wheel hub, we removed the patterns in the edge lines except the main spokes so that the edge line of the wheel pattern can maintain a dodecagonal shape in any state of the wheel transformation. The remaining flexible regions near the main spokes were clamped in the fabrication process. The final wheel prototype is presented in Fig. 2 (R and S), and the details of the fabrication procedures and materials are explained in figs. S3 to S5 and Materials and Methods.

Internal locking skeletons and tread pads are additional essential components to achieve full functionality of the wheel; internal locking structures keep the shape under lateral traction force, and tread pads absorb external impact and configure a ground contact shape (Fig. 5A). The internal locking structure made of elastic material

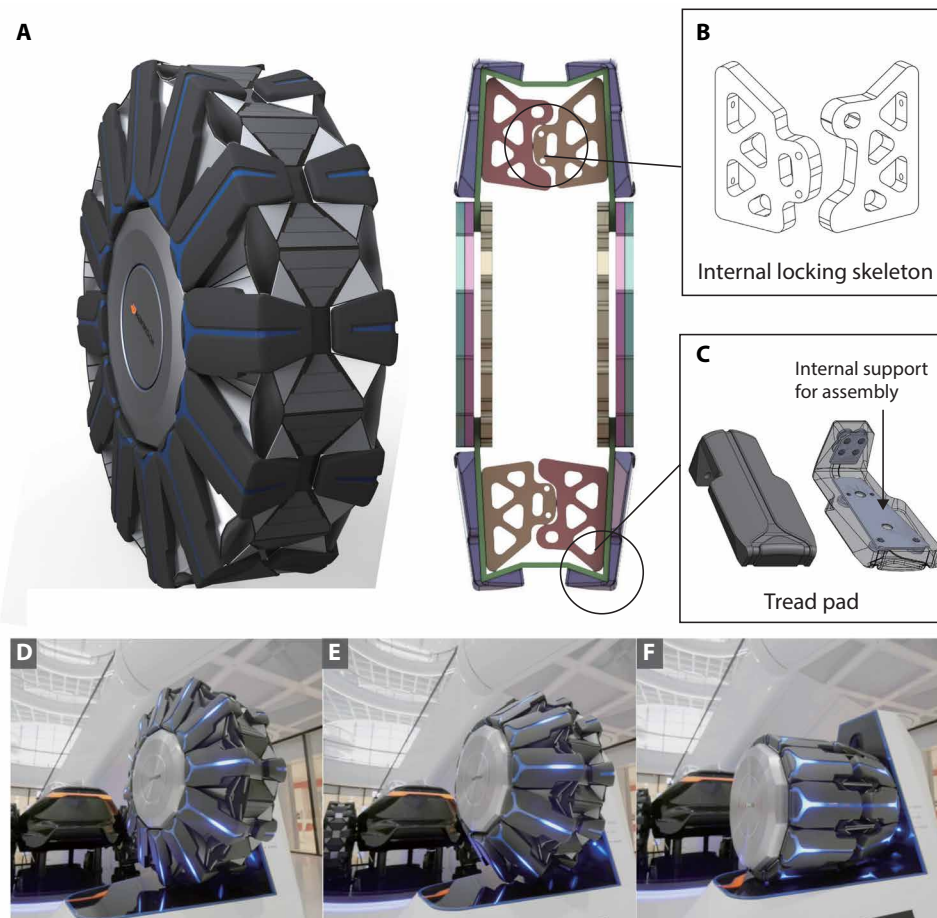


Fig. 5. Wheel components and transformation test. (A) The outer appearance and internal diagram of the wheel. (B) Internal locking skeletons to prevent wheel collapse from the lateral force and (C) tread pad to create a protuberance in the large form and a smooth surface in the small form. (D to F) Wheel transformation is verified using a linear actuation system that can change the distance between hub plates. The diameter of the wheel changed from ~0.8 to ~0.46 m

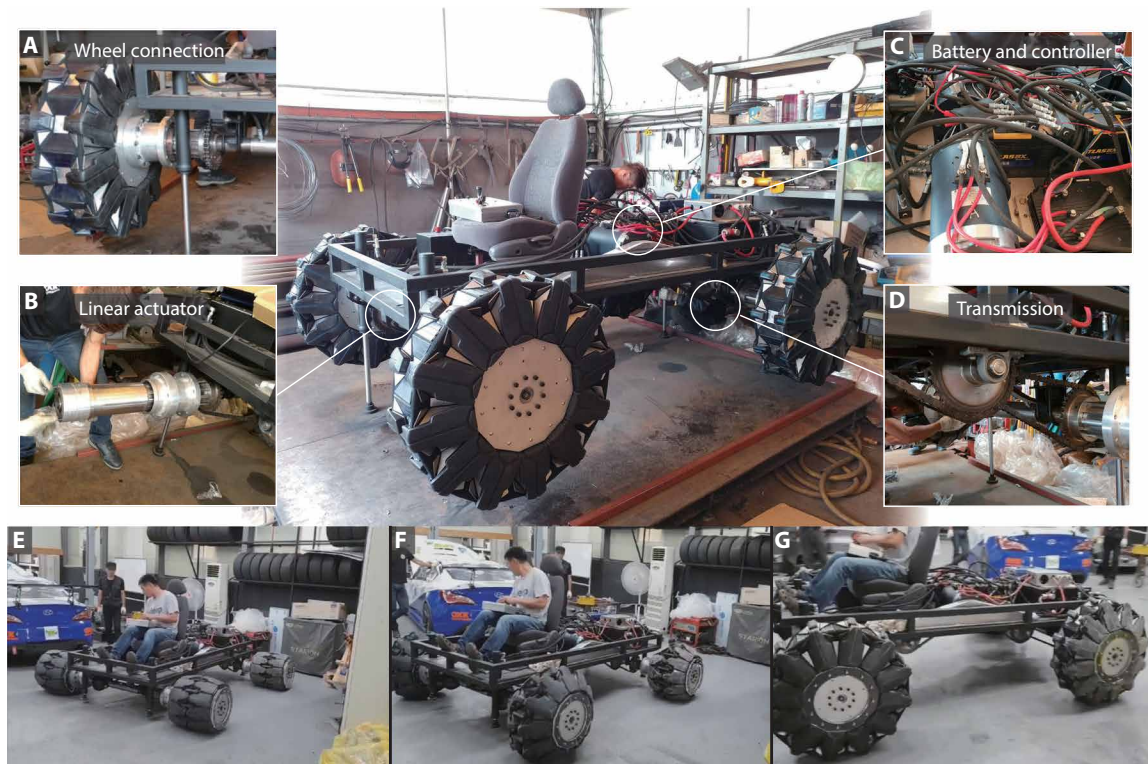


Fig. 6. Vehicle implementation and field test. (A) The wheel connection is designed for independent control of driving (wheel rotation) and transformation (wheel hub translation). (B) A hydraulic pressure system enables transformation. (C) The vehicle uses two electric motors for driving, and (D) the driving torque is transmitted through a chain. (E to G) On-site verification of wheel transformation, which can also be performed while driving.



Movie 1. Development of high-load capacity origami transformable wheel. Field demonstration and the design and fabrication procedure of the transformable wheel.

prevents collapse by impact (Fig. 5B). The tread pad is made of urethane and has an internal plastic structure for assembly (Fig. 5C). The wheel can be transformed by linear actuation that changes the distance between the wheel hub plates (Fig. 5, D to F).

An electric motor vehicle with hydraulic linear actuators for wheel transformation was constructed to evaluate on-site wheel performance (Fig. 6). The required force of the linear actuator can be approximated by a simplified model of the wheel as described in

fig. S2 and Supplementary Text. From a field test, we verified the wheel transformation in about 5 s, whereas the vehicle moved at 1 m/s (Movie 1). The vehicle was controlled manually, and the test lasted for about 30 min. We could not confirm the lifetime and maximum speed because of safety concerns. A video record of the development process and pre-field test is also included in Movie 1.

DISCUSSION

Here, we present the transition of an origami paper model into a transformable wheel prototype. We demonstrate the feasibility of applying the origami technique in a passenger vehicle. Although the wheel performances regarding speed, lifetime, vibration, and noise were not evaluated in this study, we expect that our wheel prototype cannot compete with commercially available wheels and tires at this stage of development. However, because these performance factors are closely related to material and fabrication techniques, they can be improved by further optimizing the composite membrane origami processes. For instance, we can focus on the compatibility of the origami technique with industrial rubber or tire manufacturing processes. Moreover, the lamination process is ready for integration with rubber or tire composite manufacturing, and the recently introduced airless tire technology can provide high load capacity with reinforced rubber composites. We believe that the unique characteristics of the origami technique compared with traditional structure construction will foster its development and adoption.

MATERIALS AND METHODS

The main components of the wheel include an origami body, tread pads, internal locking skeletons, and hub plates. Materials and processing methods for all components are presented in table S1, and the stepwise assembly procedure is illustrated in figs. S3 to S5. This section describes the details of fabrication procedures for the origami composite and tread pad.

Preparation of origami composite wheel body

The origami serves to maintain the shape of the wheel and produce a change in shape. To withstand high load while minimizing weight, 60 series aluminum was used for facets, and PET(1500d/1) and N-6(1260d/1) cloth was used as flexure material. Mechanical riveting was chosen as a lamination method because of high bonding strength under various external environment conditions regardless of the type of materials.

The flexure material was laser processed (Universal Laser Systems) to create holes for riveting and bolting and also trim outlines (fig. S3A). The length of the flexure of the wheel is more than 2.5 m, but the entire pattern was divided into six pieces to improve the processability. The flexure material cannot be dyed or painted because of the latex coating on the surface, but the exterior color can be customized by covering a thin colored fabric on top of the flexure material. Here, the black fabric was used for aesthetic improvement (fig. S3B).

In the lamination process (riveting process), two aluminum facets sandwich the flexure material, and rivets join the two facets. Aligning facets on both sides was a bottleneck for this process, so the riveting jig was designed to accelerate the process (fig. S3C). The flexure and fabric cover were placed on a riveting jig in which the facets were already placed. The facets were placed on top of it in line with the pattern. After placing the facet, the rivet was placed into the hole and riveted (fig. S3, D to F). For the spoke parts that have to withstand most of the load, a facet with a bent edge was used to increase the bending stiffness (fig. S3G). For aesthetic improvement, the aluminum facets were covered with the three-dimensional (3D)-printed facet (fig. S3H). The attachment of the facet and cover used a double-sided tape (5316K, Coretec) with elasticity to be sustainable against impact. After the assembly of the facet cover, the origami body was assembled in a circular form (fig. S3I).

Preparation of urethane tread pad

The tread pads play a similar role as a tire in a conventional wheel. It was assembled with the wheel body to form the final shape of the wheel, increase the friction, and absorb the shock. When the wheel is the small form, the tread pad makes the wheel in a completely cylindrical shape, making it a high-speed driving mode. When the wheel is the large form, the tread pad makes it in a protuberance shape, making it an off-road mode. Not only the tread pad uses urethane (VytaFlex 60, Smooth-on) as the main material to increase friction and absorb impact, but it also has a 3D printed skeleton part (SLA ABS-like, Shining 3D) with bolt holes to strengthen the connection with the wheel (fig. S4A). We also improved the aesthetics with two color combinations (black base with blue band line).

The blue band part was made separately and placed in the mold (fig. S4B). The molds, mold covers, and skeleton parts were assembled (fig. S4C). The urethane precursor was prepared with the black dye (SO-Strong, Smooth-on) rate of around 2% and poured into the mold (fig. S4, D and E). The initial curing requires 4 hours at 50°C (fig. S4F). After removing the tread pads from the mold, they were

trimmed and cured for another 3 days at 25°C to get better physical properties (fig. S4G).

Wheel payload measurement

The load capacity measurement was conducted on the wheel in a large form and a transition form because the capacity of the small form wheel is mainly determined by the wheel hub plate, which is presumed to have higher capacity than the large form or transition form wheel. Ektron Tek's equipment was used for the test, which includes a shaft for connecting a wheel, a linear stage, and a moving plate for applying loads (fig. S6).

The wheel payload was examined in three ways. First, in the large form, the cyclic loads of 6 ± 2 kN, 10 ± 2 kN, 12 ± 2 kN, and 14 ± 2 kN were applied in a vertical direction. Second, in the transition form, the cyclic loads of 5 ± 2 kN, 7 ± 2 kN, and 9 ± 2 kN were applied in a vertical direction. Third, in the large form, with a vertical load of 4 kN to create friction, the cyclic loads of ± 2 kN were applied in a lateral direction. The wheel is not a complete circle, so the loading direction is expected to affect the payload. Because of this reason, the vertical payload was measured by selecting two possible directions. The first direction corresponds to the main spoke in the origami pattern, and the second direction is between the two main spokes (fig. S7A). When the load experiment is performed in the first direction, one main spoke supports the load (fig. S7B), and in the second direction, two main spokes support the load (fig. S7C).

The sequence of the experiments is as follows. First, the wheel was connected to the shaft of the linear stage. After connecting, the wheel was located in the desired position (slightly contacting the ground). The moving plate rose until the load reached a target. After being stabilized, a cyclical load of ± 2 kN is applied from that position. The cyclic load-displacement data were acquired after two warm-up cycles with identical load conditions.

In the large form, with vertical load test for direction 1, the wheel shows an elastic deformation characteristic up to 10 ± 2 kN of load cycle, but the plastic deformation occurred from 12 ± 2 kN (fig. S8D, direction 1), which can be interpreted as the payload in direction 1 will be between 12 and 14 kN. For direction 2, the load was held up to 14 ± 2 kN, which means that the maximum load will be greater than 16 kN (fig. S8D, direction 2). In the transition form, with a vertical load test for direction 2, the wheel shows an elastic deformation characteristic up to 9 ± 2 kN of load cycle (fig. S8E). In the large form, the lateral load capacity test confirmed that the elasticity was maintained when a cyclical load of ± 2 kN was given under 4-kN vertical load (fig. S8F).

SUPPLEMENTARY MATERIALS

robotics.sciencemag.org/cgi/content/full/6/53/eabe0201/DC1
Text

Fig. S1. Geometrical descriptions for the flexure simple folding.

Fig. S2. A simplified model for kinetics of the wheel structure.

Fig. S3. Fabrication of the composite membrane origami.

Fig. S4. Fabrication of tread pad.

Fig. S5. The assembly of the wheel components.

Fig. S6. Payload experiment environment.

Fig. S7. Two vertical load directions of the wheel.

Fig. S8. Payload experiment result.

Table S1. Materials and processing methods of the components of the wheel.

REFERENCES AND NOTES

1. H. Kobayashi, B. Kresling, J. F. V. Vincent, The geometry of unfolding tree leaves. *Proc. R. Soc. Lond. B Biol. Sci.* **265**, 147–154 (1998).

2. L. Mahadevan, S. Rica, Self-organized origami. *Science* **307**, 1740 (2005).
3. B. Kresling, Origami-structures in nature: Lessons in designing smart materials, in *MRS Online Proceedings Library* (Springer, 2012), pp. 42–54.
4. E. Hernandez, D. Hartl, D. Lagoudas, *Active Origami: Modeling, Design, and Applications* (Springer, 2018).
5. Z. You, Folding structures out of flat materials. *Science* **345**, 623–624 (2014).
6. D. Rus, C. Sung, Spotlight on origami robots. *Sci. Robot.* **3**, eaat0938 (2018).
7. C. Laschi, B. Mazzolai, M. Cianchetti, Soft robotics: Technologies and systems pushing the boundaries of robot abilities. *Sci. Robot.* **1**, eaah3690 (2016).
8. P. Sareh, The least symmetric crystallographic derivative of the developable double corrugation surface: Computational design using underlying conic and cubic curves. *Mater. Des.* **183**, 108128 (2019).
9. N. T. Jafferis, E. Helbling, M. Karpelson, R. J. Wood, Untethered flight of an insect-sized flapping-wing microscale aerial vehicle. *Nature* **570**, 491–495 (2019).
10. J.-S. Koh, E. Yang, G.-P. Jung, S.-P. Jung, J. H. Son, S.-I. Lee, P. Jablonski, R. Wood, H.-Y. Kim, K.-J. Cho, Jumping on water: Surface tension-dominated jumping of water striders and robotic insects. *Science* **349**, 517–521 (2015).
11. Z. Zhakypov, K. Mori, K. Hosoda, J. Paik, Designing minimal and scalable insect-inspired multi-locomotion millirobots. *Nature* **571**, 381–386 (2019).
12. J. Morgan, S. Magleby, L. Howell, An approach to designing origami-adapted aerospace mechanisms. *ASME J. Mech. Des.* **138**, 052301 (2016).
13. S. D. Guest, S. Pellegrino, A new concept for solid surface deployable antennas. *Acta Astronaut.* **38**, 103–113 (1996).
14. S. Felton, M. Tolley, E. Demaine, D. Rus, R. Wood, A method for building self-folding machines. *Science* **345**, 644–646 (2014).
15. P. M. Kornatowsky, S. Mintchev, D. Floreano, An origami-inspired cargo drone, in *IEEE/RSJ International Conference on Intelligent Robots and Systems* (IEEE, 2017), pp. 6855–6862.
16. J. Faber, A. Arrieta, A. Studart, Bioinspired spring origami. *Science* **359**, 1386–1391 (2018).
17. S. Mintchev, J. Shintake, D. Floreano, Bioinspired dual-stiffness origami. *Sci. Robot.* **3**, eaau0275 (2018).
18. W. Kim, J. Byun, J.-K. Kim, W.-Y. Choi, K. Jakobsen, J. Jakobsen, K.-J. Cho, Bioinspired dual-morphing stretchable origami. *Sci. Robot.* **4**, eaay3493 (2019).
19. S.-M. Baek, S. Yim, S.-H. Chae, D.-Y. Lee, K.-J. Cho, Ladybird beetle-inspired compliant origami. *Sci. Robot.* **5**, eaaz6262 (2020).
20. Q. Zhang, X. Yang, P. Li, G. Huang, S. Feng, C. Shen, B. Han, X. Zhang, F. Jin, F. Xu, T. J. Lu, Bioinspired engineering of honeycomb structure—Using nature to inspire human innovation. *Prog. Mater. Sci.* **74**, 332–400 (2015).
21. K. Saito, S. Pellegrino, T. Nojima, Manufacture of arbitrary cross-section composite honeycomb cores based on origami techniques. *J. Mech. Des.* **136**, 051011 (2014).
22. E. Filipov, T. Tachi, G. H. Paulino, Origami tubes assembled into stiff, yet reconfigurable structures and metamaterials. *Proc. Natl. Acad. Sci. U.S.A.* **112**, 12321–12326 (2015).
23. M. B. Oliveira, C. Liu, M. Zhao, S. M. Felton, Design of a variable stiffness wrist brace with an origami structural element, in *ASME Conference on Smart Materials, Adaptive Structures and Intelligent Systems* (American Society of Mechanical Engineers, 2018), paper V002T08A009.
24. S.-J. Kim, D.-Y. Lee, G.-P. Jung, K.-J. Cho, An origami-inspired, self-locking robotic arm that can be folded flat. *Sci. Robot.* **3**, eaar2915 (2018).
25. W. Wu, Z. You, Modelling rigid origami with quaternions and dual quaternions. *Proc. R. Soc. A* **466**, 2155–2174 (2010).
26. E. Demaine, J. O'Rourke, *Geometric Folding Algorithms: Linkages, Origami, Polyhedral* (Cambridge Univ. Press, 2007).
27. T. Tachi, Geometric considerations for the design of rigid origami structures, in *Proceedings of the International Association for Shell and Spatial Structures Symposium* (Elsevier, 2010), pp. 458–460.
28. R. J. Lang, K. A. Tolman, E. B. Crampton, S. P. Magleby, L. L. Howell, A review of thickness-accommodation techniques in origami-inspired engineering. *Appl. Mech. Rev.* **70**, 010805 (2018).
29. Y. Chen, R. Peng, Z. You, Origami of thick panels. *Science* **349**, 396–400 (2015).
30. T. Tachi, Rigid-foldable thick origami. *Origami* **5**, 253–264 (2011).
31. D.-Y. Lee, S.-R. Kim, J.-S. Kim, J.-J. Park, K.-J. Cho, Origami wheel transformer: A variable-diameter wheel drive robot using an origami structure. *Soft Robot.* **4**, 163–180 (2017).
32. B. P. Rhoads, H.-J. Su, The design and fabrication of a deformable origami wheel, in *ASME International Design Engineering Technical Conferences and Computers and Information in Engineering Conference* (American Society of Mechanical Engineers, 2016), paper V05BT07A021.
33. H. Banerjee, S. Kakde, H. Ren, Orumbot: Origami-based deformable robot inspired by an umbrella structure, in *2018 IEEE International Conference on Robotics and Biomimetics (ROBIO)*, Kuala Lumpur, Malaysia, 12 to 15 December 2018, pp. 910–915.
34. D.-Y. Lee, G.-P. Jung, M.-K. Sin, S.-H. Ahn, K.-J. Cho, Deformable wheel robot based on origami structure, in *2013 IEEE International Conference on Robotics and Automation* (IEEE, 2013), pp. 5612–5617.
35. K. Kuribayashi, K. Tsuchiya, Z. You, D. Tomus, M. Umemoto, T. Ito, M. Sasaki, Self-deployable origami stent grafts as a biomedical application of Ni-rich TiNi shape memory alloy foil. *Mater. Sci. Eng. A* **419**, 131–137 (2006).
36. J. Ma, H. Feng, Y. Chen, D. Hou, Z. You, Folding of tubular waterbomb. *Research* **2020**, 1735081 (2020).
37. T. Mukhopadhyaya, J. Ma, H. Feng, D. Hou, J. Gatta, Y. Chen, Z. You, Programmable stiffness and shape modulation in origami materials: Emergence of a distant actuation feature. *Appl. Mater. Today* **19**, 100537 (2020).
38. L. Fonseca, G. Rodrigues, M. Savi, A. Paiva, Nonlinear dynamics of an origami wheel with shape memory alloy actuators. *Chaos Solitons Fractals* **122**, 245–261 (2019).
39. J. Gere, S. Timoshenko, *Mechanics of Materials*, PWS-KENT Publishing Company, ISBN 0, 534(92174), (1997).

Acknowledgments: We thank N. Chang (EMVcon, KAIST) and H. Kim (OXK) for designing and implementing the vehicle for the transformable wheel and H. Jang (Hankook Tire) for designing the appearance of the transformable wheel. **Funding:** This work was supported by Innocean Worldwide Inc. and the National Research Foundation of Korea (NRF) (NRF-2016R1A5A1938472). **Author contributions:** D.-Y.L. designed and built the wheel, developed a fabrication method, and wrote the manuscript. J.-K.K. assisted in building the wheel and experimental works. C.-Y.S. assisted in developing a fabrication method, organized fabrication facilities, and conducted experimental works. J.-M.H. assisted in developing a fabrication method and building the wheel. K.-J.C. directed the project and edited the manuscript. **Competing interests:** D.-Y.L., J.-K.K., C.-Y.S., J.-M.H., and K.-J.C. are inventors on patent (KR. 10-2136158) submitted by Hankook Tire and Technology Co. Ltd. and Seoul National University. The concept art of the result was used for a commercial film (The next driving lab project, Hankook Tire). **Data and materials availability:** All data needed to support the conclusions of this manuscript are included in the main text or the Supplementary Materials. Additional data related to this paper may be requested from the authors.

Submitted 26 July 2020

Accepted 16 March 2021

Published 7 April 2021

10.1126/scirobotics.abe0201

Citation: D.-Y. Lee, J.-K. Kim, C.-Y. Sohn, J.-M. Heo, K.-J. Cho, High-load capacity origami transformable wheel. *Sci. Robot.* **6**, eabe0201 (2021).

High-load capacity origami transformable wheel

Dae-Young Lee, Jae-Kyeong Kim, Chang-Young Sohn, Jeong-Mu Heo and Kyu-Jin Cho

Sci. Robotics **6**, eabe0201.

DOI: 10.1126/scirobotics.abe0201

ARTICLE TOOLS	http://robotics.sciencemag.org/content/6/53/eabe0201
SUPPLEMENTARY MATERIALS	http://robotics.sciencemag.org/content/suppl/2021/04/05/6.53.eabe0201.DC1
RELATED CONTENT	http://robotics.sciencemag.org/content/robotics/4/36/eaay3493.full http://robotics.sciencemag.org/content/robotics/5/41/eaaz6262.full http://robotics.sciencemag.org/content/robotics/3/20/eaau0275.full
REFERENCES	This article cites 29 articles, 7 of which you can access for free http://robotics.sciencemag.org/content/6/53/eabe0201#BIBL
PERMISSIONS	http://www.sciencemag.org/help/reprints-and-permissions

Use of this article is subject to the [Terms of Service](#)

Science Robotics (ISSN 2470-9476) is published by the American Association for the Advancement of Science, 1200 New York Avenue NW, Washington, DC 20005. The title *Science Robotics* is a registered trademark of AAAS.

Copyright © 2021 The Authors, some rights reserved; exclusive licensee American Association for the Advancement of Science. No claim to original U.S. Government Works